Int. J. Heat Mass Transfer. Vol. 31, No. 7, pp. 1497–1515, 1988
Printed in Great Britain

0017–9310/88 $3.00 + 0.00

Recirculating flows in the cross-section of a channel induction furnace

A. MOROS† and J. C. R. HUNT‡
Department of Engineering, University of Cambridge, Trumpington St., Cambridge CB2 1PZ, U.K.

(*Received* 11 *December* 1986 *and in final form* 8 *December* 1987)

Abstract—Recirculating flows in channel induction furnaces require investigation in order to understand and predict their mixing efficiency and their disadvantageous aspects, such as blocking of the channel by non-metallic materials and refractory erosion. These aspects reduce their lifetime. To understand better the physical mechanisms driving the flow, we have divided our study in two parts. In the first which is described in this paper, we analyse the two-dimensional flow in a laboratory model simulating one leg of the channel. The model consists of a 150 × 150 mm square tank containing 90 kg of mercury and powered from a 400 Hz generator. The distribution of the flux **B** was measured using search coils. Thence estimates of the distribution of the $(\mathbf{J} \times \mathbf{B})$ and its curl $\nabla \times (\mathbf{J} \times \mathbf{B})$ were derived. The results were compared with computed solutions to Maxwell's equations obtained from a finite element code. This is a decoupled problem. In that first Maxwell's equations are solved, and then, using the results for $\mathbf{J} \times \mathbf{B}$, the Navier–Stokes equations are solved. The mean flow and the turbulent intensity of the recirculating flow were measured and compared with solutions obtained from a $(k$–$\varepsilon)$ code, and approximate analyses based on a balance of the $\nabla \times (\mathbf{J} \times \mathbf{B})$ and inertia terms. Numerical experiments show how the flow pattern in the channel cross-section changes with alterations in either (i) the channel geometry or (ii) the coil length and (iii) the position of the channel to the coil.

1. INTRODUCTION

THE CHANNEL induction furnace (hereafter referred to as CIF) is an a.c. induction device for melting and holding a wide range of metals. The furnace consists of an iron core and an induction coil wound around the core. A channel containing part of the metal, forms a hydraulic loop around the induction coil. This channel is in turn connected to a larger vessel at the top, containing the bulk of the melt and is called a bath.

Electrically, the furnace is similar to a transformer in which the channel forms a single turn around the primary induction coil, Fig. 1(a). An alternating current in the primary induction coil causes an electromagnetic wave front to diffuse into the melt, resulting in large induced currents of density **J** perpendicular to the plane of the channel (Fig. 1(b)). This eventually heats the metal through the Joule dissipation

$$\int_v \frac{J^2}{\sigma} \mathrm{d}v$$

where v is the volume of the melt. The induced current interacts with the magnetic flux **B** giving rise to electromagnetic forces $(\mathbf{J} \times \mathbf{B})$.

The electromagnetic heating in the channel is only effective if the metal in the channel is mixed with the metal in the bath. This mixing is achieved only if there is flow along the axis of the channel z. Despite the widespread use of these furnaces, designers are still unable to predict whether such a flow will occur and even the direction of the flow. The reason why the flow along the channel is so uncertain is because the primary electromagnetic forces are perpendicular to the axis of the channel (i.e. in the x–y plane). There are only very weak components of force along the axis.

In developing a programme for research on the flow in channel furnaces we decided to examine in detail by experiments and computations the flow in different parts of the furnace, before attempting to make a laboratory model of an entire furnace. This approach was described in ref. [1]. The advantage of this approach is that in each part the geometry and the flow are simpler and there are certain major parameters which can be modelled, computed and then understood. When these parameters are understood it should be possible to understand and predict the flow and electromagnetic field in the entire furnace. In this paper we concentrate on the flow in the channel itself. We have also studied the flow at the junction of the channel and the bath, but this work is discussed in ref. [2].

In any section of the channel the forces are rotational, consequently recirculating motions are set up in the channel cross-section with vorticity parallel to its z-axis. The flow in these furnaces depends on: (a) geometry of the channel, channel length W, width L, height H and the shape of the channel outlets; (b) the frequency parameter $R_W = \mu\omega\sigma L_i^2$ and (c) the Reynolds number $Re = U_a\delta/\nu$, where U_a is a characteristic velocity defined by $B_0/(\mu\rho)^{1/2}$. (U_a is often referred to as the Alfven speed. This is not related to

† Present address: BP Research Centre, Chertsey Road, Sunbury-on-Thames, Middlesex TW16 7LN, U.K.

‡ Also Department of Applied Mathematics and Theoretical Physics, University of Cambridge, Silver St., Cambridge, U.K.

NOMENCLATURE

B	magnetic flux vector
B_0	a characteristic value of the magnetic field [mT]
C_μ	turbulent viscosity constant
F	electromagnetic force vector
f	frequency of the magnetic field [Hz]
g	gravitational acceleration
I_c	coil current [A]
J	current density vector
J_0	characteristic value of the current density [A m^2]
L_i	characteristic length [m]
L	channel width [m]
P_1, P_2	dimensionless parameters
Pr	magnetic Prandtl number
Re	Reynolds number, $U_a\delta/\nu$
Re_m	magnetic Reynolds number
ΔT	temperature difference
U_a	characteristic velocity, $B_0/(\mu\rho)^{1/2}$ [m s^{-1}]
U	velocity vector
U	mean velocity in x-direction
u', v'	r.m.s. values of the fluctuating velocities
V	mean velocity in y-direction.

Greek symbols

β	coefficients of expansion
δ	skin depth, $(2/\mu\omega\sigma)^{1/2}$
ε	viscous dissipation
κ	turbulent kinetic energy
μ	magnetic permeability ($4\pi \times 10^{-7}$)
ν	kinematic viscosity
ν_t	turbulent viscosity
ρ	density
σ	electrical conductivity
τ	shear stress
τ_ε	turbulent integral time scale
ϕ	phase angle
ω	angular frequency.

Subscripts

$+$	dimensionless quantities based on the friction velocity
j, b	current and magnetic flux
x, y	x- and y-directions.

the speed of the Alfven wave, but the same expression gives a characteristic velocity.) B_0 is the strength of the applied magnetic field, μ the magnetic permeability, ρ the metal density and $\delta = (2/\mu\omega\sigma)^{1/2}$ the skin depth. In general the flow is turbulent. A typical value of Re is about 10^5.

The degree of mixing between the metal in the channel and the bath depends on the variation of the electromagnetic forces and the flow along the length of the channel. This is one of the differences between the CIFs and the coreless furnace where the degree of mixing is largely independent of the shape of the furnace [3]. However, the intensity of the mean flow in both cases is related to the coil current and scales on the Alfven speed, as predicted in ref. [4] for the coreless furnace.

In CIFs the ratio of the electromagnetic and buoyancy forces can be defined by the two dimensionless parameters [5], similar to Reynolds and Grashof numbers

$$P_1 = \frac{B_0^2 L_i^2}{\mu\rho\nu^2} = \frac{U_a^2 L_i^2}{\nu^2}, \quad P_2 = \frac{g\beta\Delta T L_i^3}{\nu^2}$$

where L_i is a characteristic length.

For a CIF with symmetric outlets, such as that of Fig. 1(a), taking L_i and U_a along the channel axis, these numbers are of the same order. However, in the plane (x–y) of the channel where strong flows exist the electromagnetic forces are much greater than the buoyancy forces.

A theoretical study of an idealized CIF was performed by Mestel [6], but most of the studies on the flow in realistic geometries of CIFs, have been very empirical. They have mainly been carried out in large-scale furnaces and concentrated on how to create flows along the channel, by modifying the channel outlets [7–10]. As far as the small-scale laboratory work is concerned, the most systematic studies have been conducted by Butsenieks *et al.* [11] and Arefev *et al.* [12] on horizontal models operating with either mercury or woods metals. They were mainly concerned with flow visualization along the channel and the only parameters measured were the temperature and current density.

In this paper we analyse the distribution of electromagnetic forces and the flow (experimentally and numerically) using a (k–ε) model, in the cross-section of an idealized model, simulating one leg of the channel. In this case we eliminate any flow perpendicular to the channel plane, so we are able to study the strong eddying motion on the channel plane. This is now a two-dimensional problem. Since the eddying motion on the channel plane is much stronger than any flow along the channel one has to know the magnitude and direction of rotation of those eddies. It is important to understand the mechanism of these flows and how they interact with the flow along the channel. In the past (k–ε) models have been used for the studies of metal flow in coreless furnaces [3, 13, 14] but no attempt has been made for the case of channel furnaces.

In Section 2 we describe the experimental model, in Section 3 the computer code and in Section 4 we discuss the distribution of the electromagnetic forces.

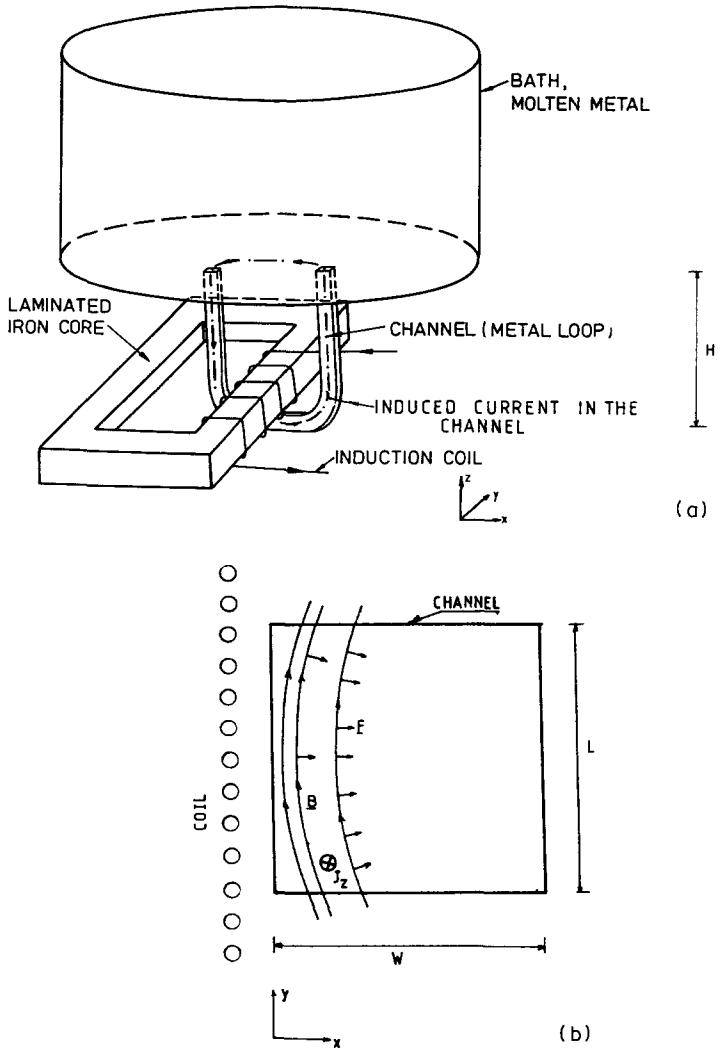

FIG. 1. (a) Channel induction furnace. (b) Channel cross-section.

In Section 5 we present and discuss the measurements and computations of the flow field and in Section 6 the influence of the channel aspect ratio on the flow pattern.

2. LABORATORY MODEL

The salient features of the apparatus are shown in Fig. 2. Essentially it consists of a low-permeability ($\mu < 1.05$) stainless steel tank 15 × 15 cm square cross-section and 30 cm high, filled with mercury to simulate the melt. To balance the induction heating of the mercury, the system is cooled by cold water from a gallery, pouring down the outside of the tank wall. The water enters the gallery via two diametrically opposite 10 mm i.d. circular inlets and flows in the periphery of the tank. The upper and lower base of the tank and the gallery are connected with stainless steel flanges. This technique of cooling is effective and allows the apparatus to run continuously with an average temperature in the mercury of 32°C. The temperature gradients in the mercury were less than 2°C.

The tank is surrounded by a laminated iron core on which a 16 turn water-cooled coil is wound around one of its legs. The coil is supplied from a single-phase 400 Hz generator. In order to recirculate the current induced in the mercury a copper bar connects the top and bottom of the tank (Fig. 2). The parameters involved in the model with their numerical values are shown in Table 1.

The investigation of the velocity field in the liquid metal recirculating flows requires:

(a) direction of the flow field;

(b) typical values of the mean and fluctuating velocities.

The flow in the channel was investigated using the drag anemometer, described in ref. [15], which measures the force experienced by a perforated sphere of

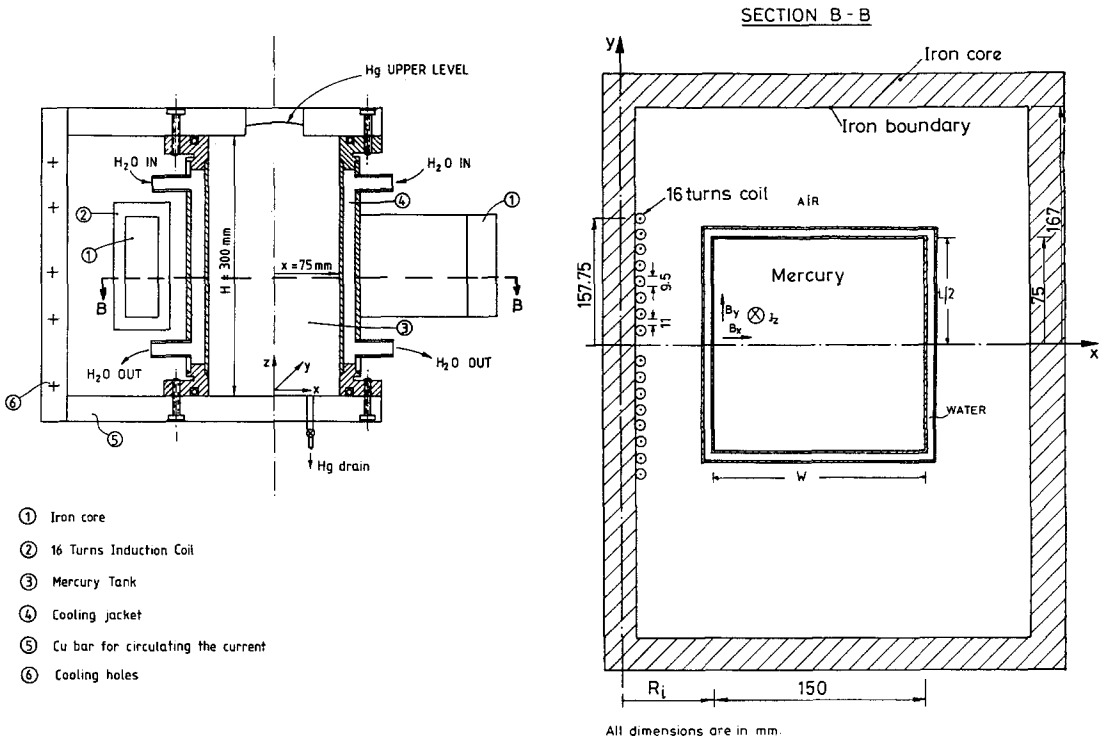

FIG. 2. Laboratory model. Single channel leg.

6 mm o.d. The velocities were then calculated from the linearized formula $\hat{E}_i = C\hat{U}_i$, where $\hat{E}_i$ is the measured voltage (which is proportional to the force) in the i-direction and C the calibration coefficient. The systematic error for the calculation of the mean velocities is about 10% for mean velocities greater than 5 cm s^{-1} and of the order of 49% for velocities less than 4.0 cm s^{-1}. The processing of the signal and the calibration of the probe have been discussed in ref. [15]. The probe can also measure turbulent fluctuations, up to a frequency of 30 Hz. Near the boundaries the sphere was replaced by a thin (1 mm) solid rod.

3. NUMERICAL MODEL FOR THE FLOW CALCULATIONS

The fluid motion in the channel, as has already been discussed, is turbulent. After the mean motion has been reached a steady-state condition (i.e. ignoring start-up effects), it may be represented by the Reynolds or time-averaged vectorial form of the Navier–Stokes equations, together with the equation of the conservation of mass

$$\rho(\mathbf{U}\cdot\nabla)\mathbf{U} = \nabla p + \nabla\cdot\tilde{\tau} + \mathbf{F} \tag{1}$$

$$\nabla\cdot\mathbf{U} = 0. \tag{2}$$

Here ρ is the density, $\mathbf{U}$ the mean velocity, $\mathbf{F}$ the body force per unit volume, $\tilde{\tau}$ the Reynolds stress tensor and p the pressure. Except at very low frequencies, in metallurgical M.H.D. the turbulence is neither affected by the fluctuating part of the force, not by any electromagnetic damping [4, 16]. However, the electromagnetically driven flows are complex turbulent flows with high levels of turbulence, large-scale unsteadiness and intense wall jets at the side walls. Although not all of these aspects of the turbulent flow

Table 1. Parameters and numerical values involved

δ	skin depth	25 mm
W	channel length	150 mm
L	channel width	150 mm
Re	Reynolds number	2.1×10^5
Re_m	magnetic Reynolds number	0.0302
Pr	Prandtl number	0.02
$B_0/(\mu\rho)^{1/2}$	Alfven velocity	0.28 m s^{-1}
I_c	coil current	540 A
f	applied frequency	400 Hz
ρ	density	1.355×10^4 kg m^{-3}
ν	kinematic viscosity	

Table 2. Numerical values of the turbulent constants

C_D	C_1	C_2	C_μ	C_ε	κ	E
1.0	1.4	1.9	0.09	1.3	0.42	9.8

can be modelled by simple turbulent models, the $(k$–$\varepsilon)$ model can describe many aspects of the flow. It is also easy to use. This model entails the solution of transport equations for the kinetic energy of the turbulence and its dissipation rate. The Reynolds stresses are related to the rate of strain using an eddy viscosity hypothesis [17]

$$\frac{\tilde{\tau}_{ij}}{\rho} = \nu_t\left(\frac{\partial \bar{U}_i}{\partial x_j}+\frac{\partial \bar{U}_j}{\partial x_i}\right)-\frac{2}{3}k\delta_{ij}. \tag{3}$$

The eddy viscosity ν_t is then related to the turbulent kinetic energy k and the rate of viscous dissipation ε per unit mass

$$\nu_t = C_\mu\frac{k^2}{\varepsilon} \tag{4}$$

where C_μ is a parameter that is assumed to be constant.

The transport equation for k is based on the turbulent kinetic energy equation, while the transport equation for ε is based on the more approximate assumption, that local isotropy prevails. The differential transport equations for k and ε used in these computations are in their standard form, which can be found in numerous textbooks (i.e. Rodi [17]). The numerical values of the constants involved in the k and ε equations used in this model are shown in Table 2.

The general procedure consists, in first computing the electromagnetic forces by solving Maxwell's equations which can be *decoupled* from the fluid equations since $|U \times B|/|E| \approx 10^{-2}$. Maxwell's equations were solved using a finite element scheme developed by Waddington [18] (for the solution procedure see also ref. [1]). The computed electromagnetic forces were then introduced in the momentum equation (1) as an input at the nodes of the finite difference grid. For this problem a (31 × 16) computational grid was used. The equations were discretized using a central difference scheme for the diffusion terms and a power law difference scheme for the convection ones. The set of simultaneous algebraic equations were then solved iteratively using the 'SIMPLE ALGORITHM' described by Patankar [19].

The boundary conditions used are given below.

(1) At the solid boundaries the standard non-slip condition was applied. Near the boundaries where sharp gradients occur, the outer solution is matched using well-established wall functions [20]. This is a convenient technique to avoid computing the details of the flow near the wall. It is not satisfactory when there is jet-like flow along the wall. In these flows where there are two counter-rotating vortices and as will be seen in the next section the flow is driven by the $(\mathbf{J} \times \mathbf{B})$ forces, we would obtain a good solution even with a non-slip condition. The wall conditions do not have much effect on the general flow.

(2) At the axis of symmetry the gradients of all quantities are zero, except the transverse velocity $\bar{V}$ which is itself zero.

4. ELECTROMAGNETIC FORCES

Because the applied current density $\mathbf{J}$ and the induced flux $\mathbf{B}$ vary sinusoidally with time

$$\mathbf{J}(t) = \mathbf{J}_0\cos(\omega t+\phi_j)$$
$$\mathbf{B}(t) = \mathbf{B}_0\cos(\omega t+\phi_b) \tag{5}$$

the electromagnetic forces consist of a mean component and an oscillating one fluctuating at twice the applied frequency

$$\mathbf{F}(t) = \frac{J_0B_0}{2}\times\{\cos(\phi_j-\phi_b)+\cos 2(\omega t+\phi_j+\phi_b)\}. \tag{6}$$

Due to the high inertia of the fluid only the mean component needs to be considered [4]

$$\bar{\mathbf{F}} = \frac{\omega}{2\pi}\int_0^{2\pi/\omega}\mathbf{F}(t)\,dt. \tag{7}$$

Because the model is two-dimensional the main components of the magnetic flux are $B \equiv (B_x, B_y, 0)$ and also $\partial/\partial z = 0$. The current density has components, $J \equiv (0, 0, J_z)$. The two components of the magnetic flux and their phases were measured using search coils. The measurements were compared with results obtained from finite element computations of the electromagnetic field [1, 18]. Figure 3(a) shows the spatial distribution of the axial component of the magnetic flux b_x with $y/(L/2)$ and Fig. 3(b) the decay of the transverse component b_y with x/W. This decay is due to the skin effect.

The components of the force $\bar{\mathbf{F}}$ can be measured indirectly from

$$\bar{\mathbf{F}}_x = -\frac{b_y}{\mu}\left\{\frac{\partial b_y}{\partial x}-\frac{\partial b_x}{\partial y}\cos(\phi_x-\phi_y)+b_x\frac{\partial \phi_x}{\partial_y}\sin(\phi_x-\phi_y)\right\} \tag{8}$$

$$\bar{\mathbf{F}}_y = \frac{b_x}{\mu}\left\{\frac{\partial b_y}{\partial_x}\cos(\phi_x-\phi_y)+b_y\frac{\partial \phi_y}{\partial x}\sin(\phi_x-\phi_y)-\frac{\partial b_x}{\partial y}\right\} \tag{9}$$

where b is the magnitude of the magnetic flux and ϕ its phase difference relative to the coil current. The gradients were estimated from the numerical differentiation of b and ϕ.

It is important to emphasize that in these flows as in any confined flows the rotational part of the force

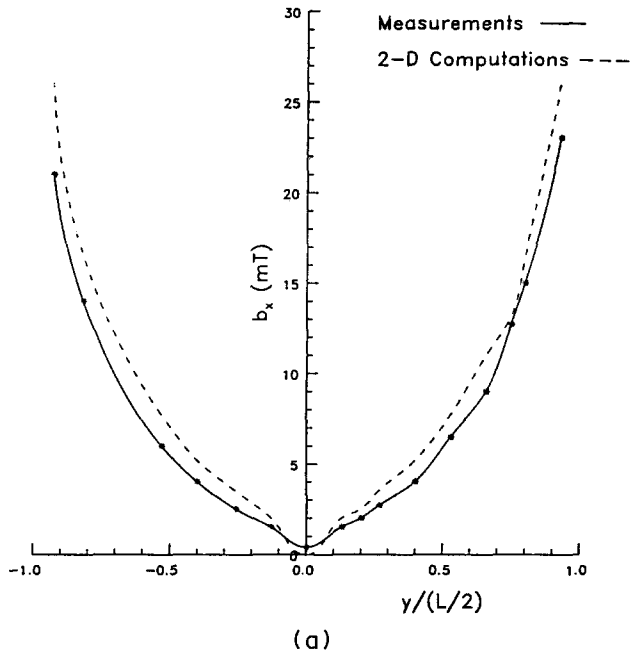

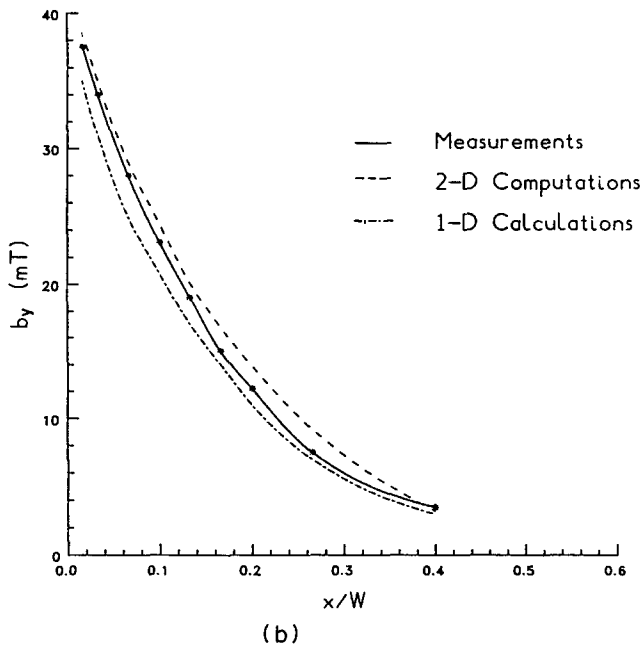

FIG. 3. (a) Variation of the axial magnetic flux density with $y/(L/2)$, at $x/W = 0.066$: $I_c = 560$ A, 400 Hz. (b) Variation of the transverse magnetic flux with x/W in the middle plane (i.e. $y/(1/2) = 0.0$): $I_c = 560$ A, 400 Hz.

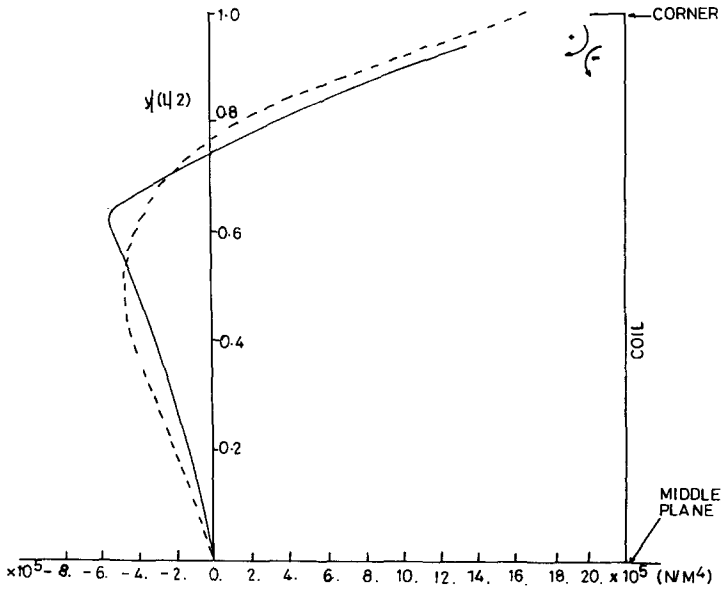

FIG. 4. Variation of the curl $(\overline{\mathbf{J} \times \mathbf{B}})$ with $y/(L/2)$ at $x/W = 0.03$: $I_c = 560$ A.

curl $\bar{\mathbf{F}}$, drives the fluid motion. The spatial distribution of curl $(\overline{\mathbf{J} \times \mathbf{B}})$ with $y/(L/2)$ is shown in Fig. 4. The overall distribution of the curl $\bar{\mathbf{F}}$ in the half channel cross-section is shown in Fig. 5. The sign of the curl changes, moving from the middle plane towards the side wall. The concentration of the $-$ve curl $\bar{\mathbf{F}}$ near the inner wall for symmetric channel/coil geometries is a feature of the channel furnaces and *has not* been observed in the coreless furnaces [21]. In the latter the sign of curl $\bar{\mathbf{F}}$ is uniform for any coil/melt geometry, except when shields are introduced [22], while in channel furnaces the sign of the curl depends on the coil/channel arrangement. The $-$ve sign near the middle plane implies that the vorticity of the fluid (i.e. mercury) should tend to change its sign from what it was as it leaves the corner region. This does not imply that it actually rotates in the opposite direction.

5. VELOCITY MEASUREMENTS AND COMPUTATIONS

With the coil current at 540 A, 400 Hz the two velocity components $\hat{U}$, $\hat{V}$ were measured over a 10 mm mesh. The mean components of the velocity $\bar{U}$ and $\bar{V}$ were obtained by averaging the signal in a microprocessor voltameter. This instrument provides the mean and the corresponding standard deviation σ_x, σ_y. The two components $\bar{U}$, $\bar{V}$ were added vectorially and the mean flow distribution is shown in Fig. 6(a). Figure 6(b) shows the computed stream-

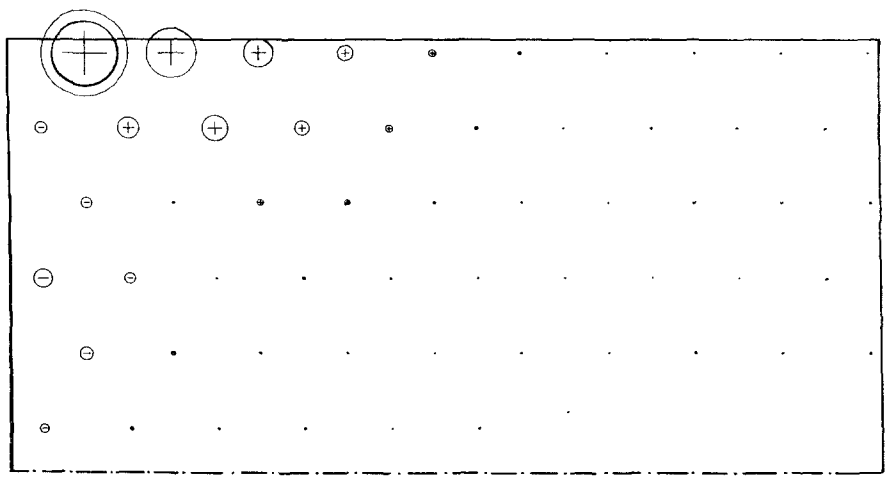

FIG. 5. Circles of the computed curl $\mathbf{F}$ over half of the channel cross-section. The different sizes of the circles denote different strength. The maximum value is denoted by a double circle and is 1.8×10^6 N m^{-4}.

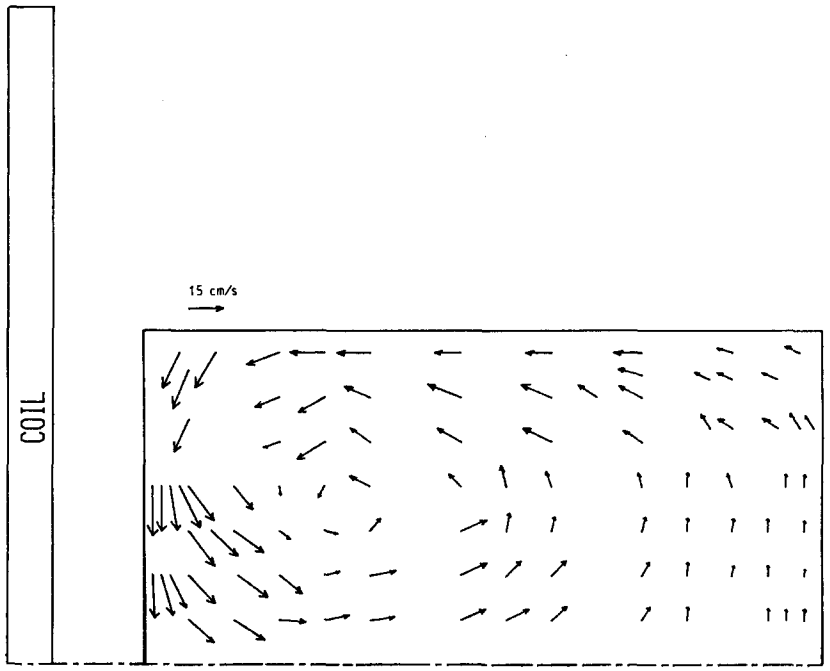

(a)

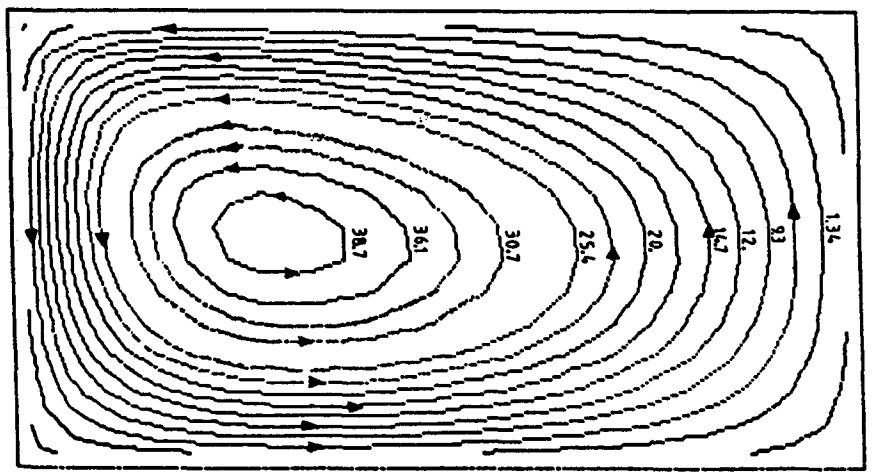

(b)

FIG. 6. (a) Measured recirculating flow pattern : $I_c = 560$ A, 400 Hz. (b) Computed streamlines. The values of the stream functions are in $m^2\ s^{-1}$: $I_c = 560$ A, 400 Hz.

lines. The experimental errors in measuring the velocity were about 14% near the plane of symmetry and the outer wall where an instability of the core jet occurred and less than 10% near the inner and side walls. The experimental values were checked during four consecutive weeks and were found to be consistent. This reveals that for symmetric coil/channel geometries the flow consists of two counter-recirculating eddies which are symmetric with respect to the plane of the channel. The recirculating eddies are driven by the curl of the body force $\nabla \times \bar{\mathbf{F}}$, which has its maximum value near the corner of the inner wall close to the induction coil. The fluid gains its vorticity by passing through the corner region. Then it flows along the inner wall and mixes with fluid of *opposite* vorticity in the core region. By this diffusion of vorticity, the net vorticity in the flow when it returns along the side wall is very small. Figure 7 shows the mean axial velocity profile across the eye of the vortex. The solid line with the dots represents the experimental measurements.

The measured values of the $\bar{U}$ component were

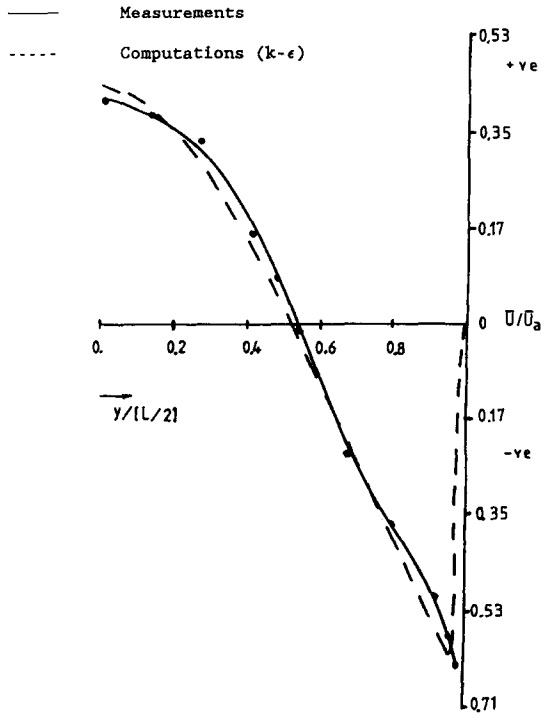

FIG. 7. Axial velocity profiles across the eye of the vortex: I_c = 560 A, 400 Hz.

checked against the necessary continuity condition

$$\int_0^{L/2} \bar{U}\,dy = 0. \tag{10}$$

In fact the continuity was satisfied to within 6%. A greater discrepancy in the net volume flow, of about 18%, occurred when the $\bar{V}$ component of the velocity was checked near the outer wall. This error is just consistent with the experimental errors discussed above.

In each recirculating cell, there is a central region ($y/(L/2) \approx 0.4$–0.8) where the axial velocity is a linear function of y, and a shear layer near the wall. The variation of the transverse velocity $\bar{V}$ with x/W at $y/(L/2) = 0.4$ is shown in Fig. 8. Figure 9 shows the velocity profiles of the transverse mean component $\bar{V}$ at different distances of $y/(L/2)$. The discrepancy between the measured and computed profiles in the near wall region is possibly due to the coarse mesh used in the computations (which was one-fifth of the skin depth) and due to the extrapolation through the use of the wall functions on the boundaries. Near the axis of symmetry the velocity profiles tend to flatten out due to the opposite sign of $\mathbf{V} \times \bar{\mathbf{F}}$ as discussed in the preceding section.

From these results one can see that the flow is

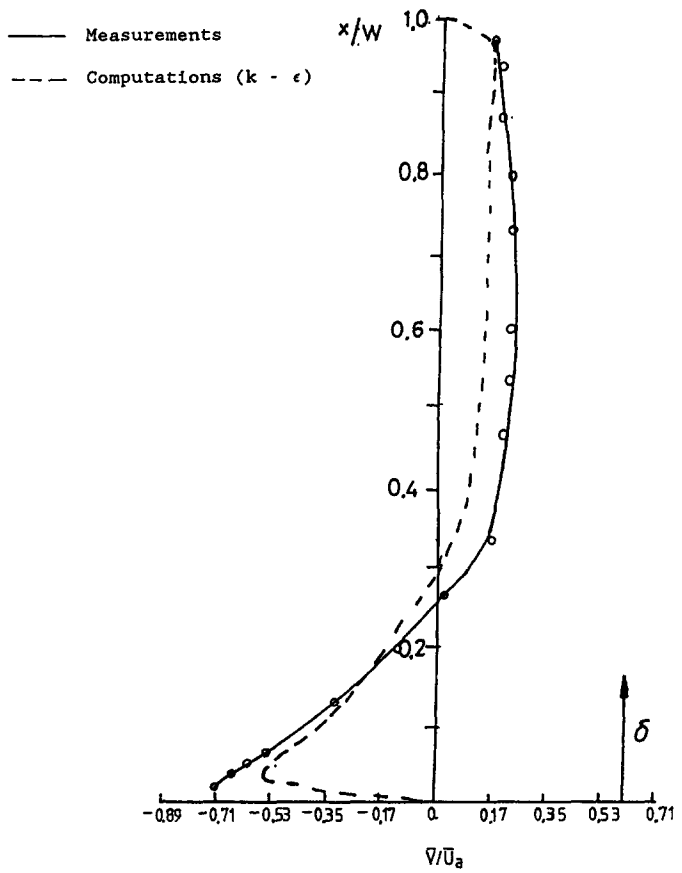

FIG. 8. Transverse velocity profiles at $y/(L/2) = 0.4$: I_c = 560 A, 400 Hz.

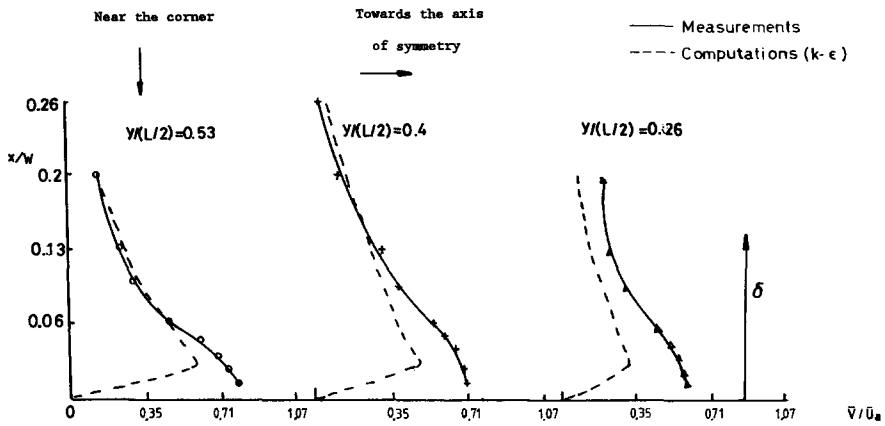

FIG. 9. Transverse velocity profiles: $I_c = 560$ A, 400 Hz.

mainly governed by the vorticity added to the fluid particles from the action of $\nabla \times \bar{\mathbf{F}}$ and its diffusion in the core. It is not controlled by the solid boundaries. Therefore, one would expect that even simple models will give a reasonable flow field. Such simple models of uniform eddy viscosity were used in ref. [5]. The results show a good agreement with the measurements and the computations up to the distance $x \approx 3\delta$ from the inner wall.

Approximate analysis based on the balance of the electromagnetic and inertia forces yields an estimate of the flow in the corner region of the inner and side wall (Appendix). The balance implies that

$$\nabla \times (\mathbf{U} \cdot \nabla)\mathbf{U} \approx \frac{1}{\rho} \nabla \times \bar{\mathbf{F}}. \tag{11}$$

Then on performing a double integration and using the fact that the vorticity of the flow entering the region is small, similar to the one used in ref. [21], we find

$$U^2 \approx \frac{2}{\rho} \int_s \nabla \times \bar{\mathbf{F}} \, ds \tag{12}$$

where s is the area of the corner region. In these types of flow this method does not give an accurate estimation of the velocity along the inner wall (Fig. 10). Equation (12) shows that the vorticity is controlled by the distribution of curl $\bar{\mathbf{F}}$, and not by shear stresses. Therefore, the sign of the velocity depends on the numerical value of $\nabla \times \bar{\mathbf{F}}$. However, this approach gives some estimation of the spatial distribution, and a better estimation of the velocity than the simple scaling argument

$$U \approx U_a = B_0/\sqrt{\mu\rho}. \tag{13}$$

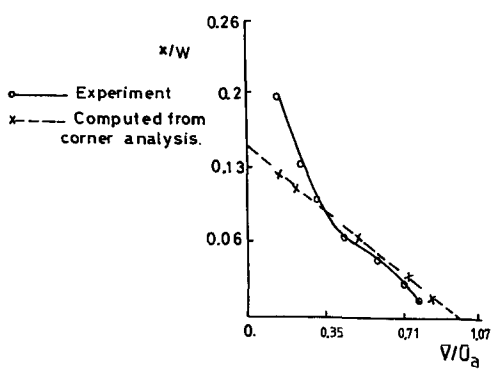

FIG. 10. Theoretical and experimental variation of the mean velocity $\bar{V}$ with x/W at $y/(L/2) = 0.6$: $I_c = 560$ A, 400 Hz.

An important feature of the flow is that, as the coil current increases, the velocity in the shear layer $\mathbf{U}_{sh}$ increases linearly but the structure (e.g. the form of the velocity profiles) of the mean flow remains unchanged. This reveals that the flow is controlled by shear stresses associated with high Reynolds number turbulence as has been suggested by many researchers [4, 23], and not by viscous effects where velocity would have been proportional to I^2. Similar relations have been observed by researchers in the coreless furnaces [16].

A profile of the r.m.s. of the axial component u as a ratio of the core mean velocity is plotted in Fig. 11. The solid line represents the values measured in the laboratory model and the dotted line those computed using the $(k$–$\varepsilon)$ code.

Measurements of the autocorrelation function $R(\tau)$ and the Fourier spectrum provides a basis for deeper insight into the properties of the turbulence. Figure 12(a) shows the Fourier spectrum of the horizontal velocity $\hat{U}$, near the side wall. This shows that the frequencies of the fluctuations are below 15 Hz. A characteristic frequency of ≈ 0.3 Hz is observed. This corresponds to the circulation time of the mean flow and is approximately equal to $L/\bar{U}$, where L is the path around a closed streamline. This integral time scale is much greater than the turbulent integral time scale $\tau_\varepsilon \approx 0.7$ s, which was calculated from the autocorrelation $R(\tau)$ (Fig. 12(b))

$$\tau_\varepsilon \approx \int_0^\infty R(\tau) \, d\tau. \tag{14}$$

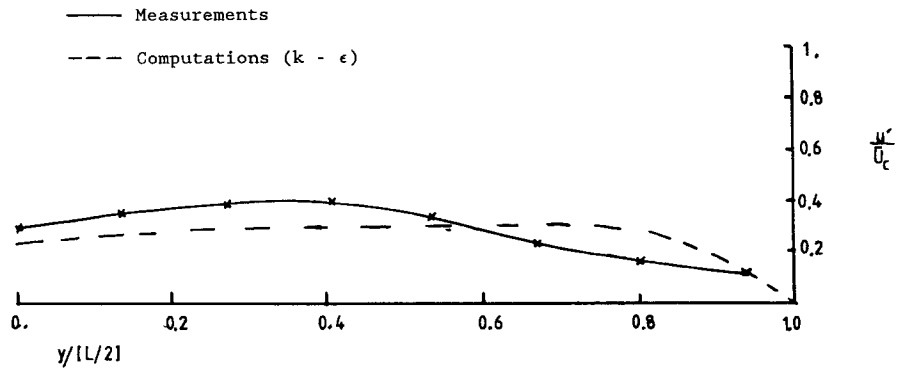

FIG. 11. Turbulent intensity across the eye of the vortex: $I_c = 560$ A, 400 Hz.

Long time scale fluctuations are characteristic of many recirculating flows. It is not clear whether the long time periodicity is due to turbulence or due to the mean flow.

During the measurements of the transverse velocity $\hat{V}$ near the mid-plane of the channel a switching mechanism in the direction of $\hat{V}$ was observed. The reason of this unstable nature of the mean flow is not clearly understood at present. A likely cause lies in the unstable nature of the core jet, possibly attributed to the Coanda effect. Sivasegaram and Whitelaw [24] in their work on jets in confined spaces, found that it was impossible to determine precisely the time scale of the switching effects.

Figure 13 shows the contours of the pressure distribution in the channel. The values show the static pressure difference relative to the bottom point on the left-hand corner, which was set to be 1 bar at the beginning of the calculations. The values on the contours are in $N\,m^{-2}$. It can be seen that the pressure has its minimum values near the corner where the electromagnetic forces have their maximum value. In the practical channels, operating say with aluminium, if the static pressure in the channel drops below the vapour pressure of the volatile species in the melt, cavities will be formed. Cavitation in the flow close to the boundaries are the prime cause of refractory erosion. This phenomenon has been discussed by Lillicrap [25]. From the computed pressure distribution one can see the possible regions for the formation of the cavities are the two corners. Therefore, the designer of the practical channels, should aim for channels with no sharp corners in the inner wall.

6. INFLUENCE OF CHANNEL CROSS-SECTION ON THE FLOW PATTERN

During early experimental work, it was noted that a small asymmetry (< 5 mm) between the plane of the channel and that of the induction coil (Fig. 2) lead to asymmetric electromagnetic fields and consequently asymmetric flow in the channel. In order to examine these effects more carefully and also to investigate the influence of the channel aspect ratio W/L on the flow field, three more cases were studied numerically.

(1) Symmetric channel to coil geometry, similar to the one studied in the previous section, but with channel dimensions of: (a) $W = 2\delta$ and $L/2 = 3\delta$; (b) $W = \delta$ and $L/2 = 2\delta$.

(2) In this case the channel was displaced to the left of the coil plane by 20 mm, with a reduced pitch. The channel dimensions were the same as those given in Table 1 ($W = 6\delta$, $L = 6\delta$).

The calculation procedure was the same as the one described in Section 3 and the coil current for the following calculations was also 540 A, 400 Hz. The streamlines for the case of $W = 2\delta$ and $L/2 = 3\delta$ are shown in Fig. 14. Comparing Figs. 6 and 14, it is clear that for $W = 2\delta$ the flow changes direction. A better understanding of the mechanism, can be obtained from the examination of the distribution of curl $\bar{\mathbf{F}}$ (Fig. 15), which is the driving force of the flow. In this case the main component of curl $\bar{\mathbf{F}}$ of $-$ve sign is concentrated along the inner wall. The positive part is much weaker on the side and on the outer wall. Consequently the fluid particles rotate in the direction opposite to that of $W = 6\delta$. For $W = 6\delta$ the main component of curl $\bar{\mathbf{F}}$, as has already been discussed in Section 4, has $+$ve sign. By reducing the channel length W the $+$ve curl diminishes and the only considerable component is the $-$ve one. The counter-recirculating eddy at the top right-hand corner is due to the $+$ve curl in this region.

Figures 16(a) and (b) show the streamlines and the force distribution, respectively, for $W = \delta$ and $L/2 = 2\delta$. In this case since the forces are surrounding the metal in the channel, they tend to pinch it. However, the forces in the inner wall are much greater than those in the outer wall, and cannot be balanced by the pressure gradient and recirculating motion still exists. This contradicts the speculation of some workers [25, 26] that for channel lengths equal to one skin depth the $\nabla \times \bar{\mathbf{F}} \approx 0$ and the forces will squeeze the metal out of the channel. The interesting phenomenon here, is that there are very weak low velocities near the axis of symmetry, due to the weak counter-recir-

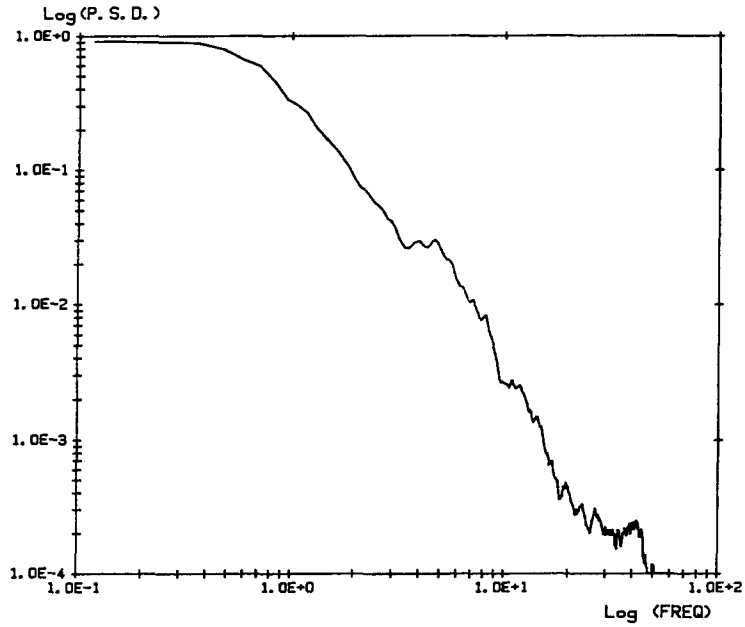

HALF POWER SPECTRAL BANDWIDTH = 1.3411 Hz

(a)

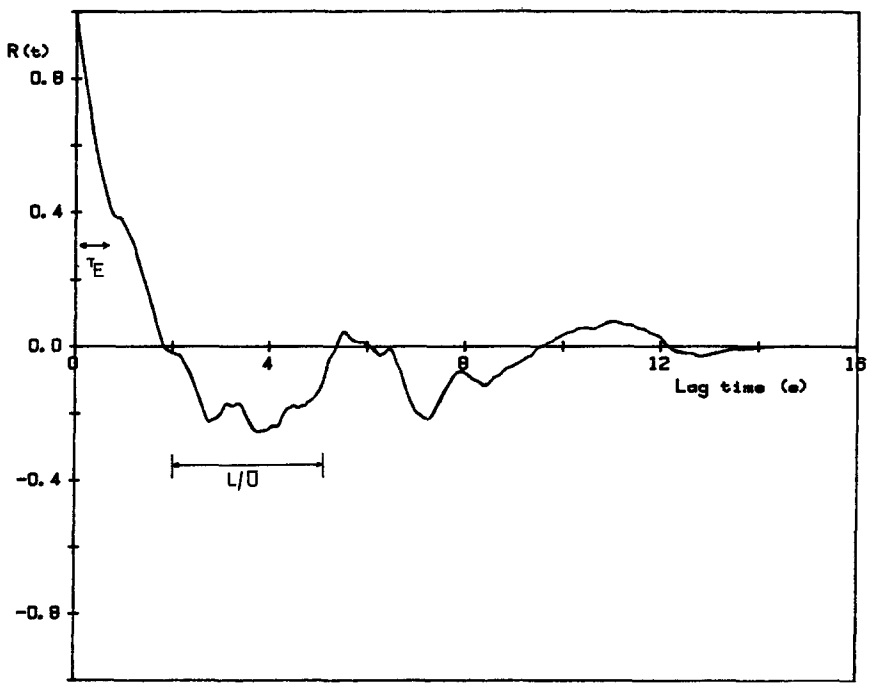

INTEGRAL TIME SCALE = 744 ms

(b)

FIG. 12. (a) Spectrum of the axial component u' at $x/W = 0.2$ and $y/(1/2) = 0.94$ using the drag prob $I_c = 560$ A, 400 Hz. (b) Autocorrelation of the axial velocity component at the same point.

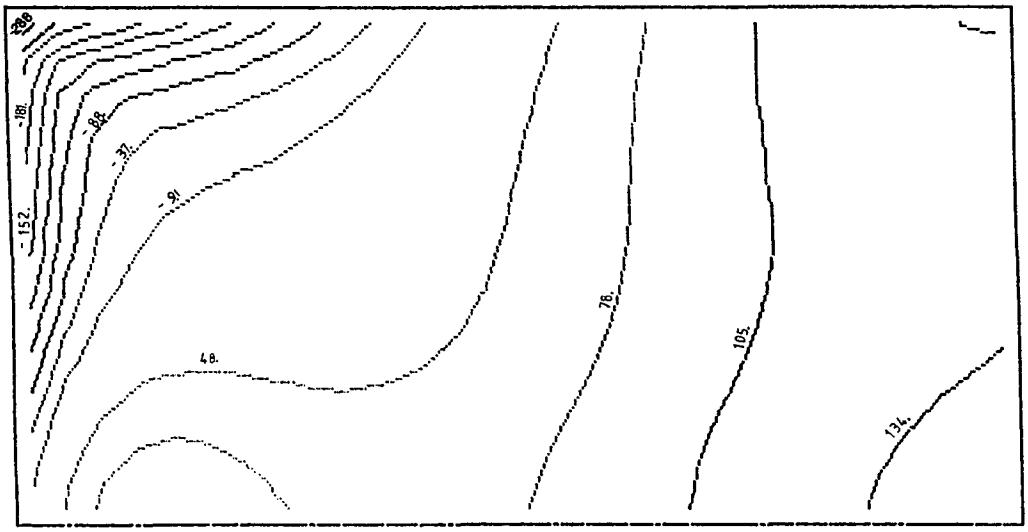

FIG. 13. Contours of the computed pressure difference in N m^{-4}: I_c = 560 A, 400 Hz.

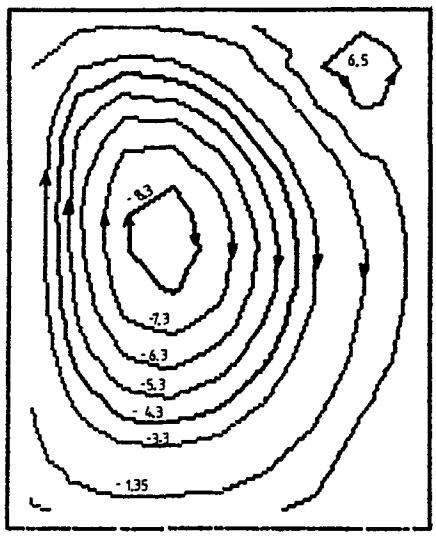

FIG. 14. Computed streamlines for $W = 2\delta$, $L/2 = 3\delta$. Values in m^2 s^{-1}: I_c = 560 A, 400 Hz.

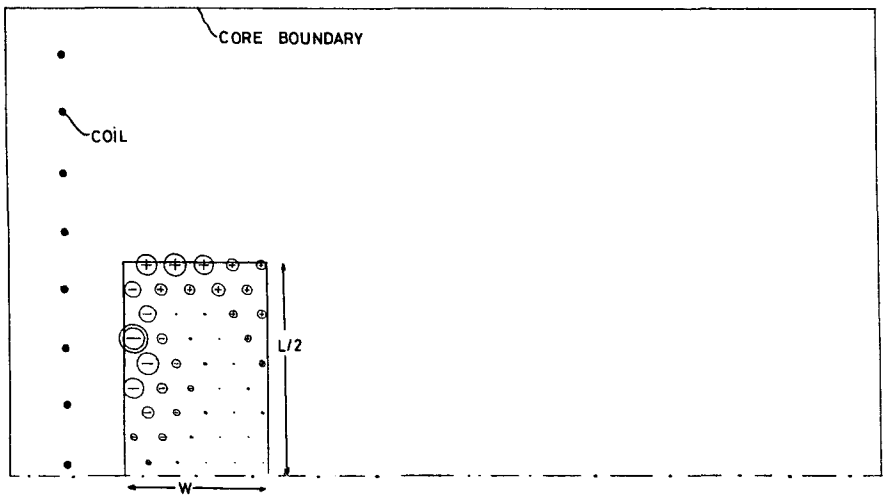

FIG. 15. Distribution of curl $\bar{\mathbf{F}}$ for channel of $W = 2\delta$, $L/2 = 3\delta$: I_c = 560 A, 400 Hz.

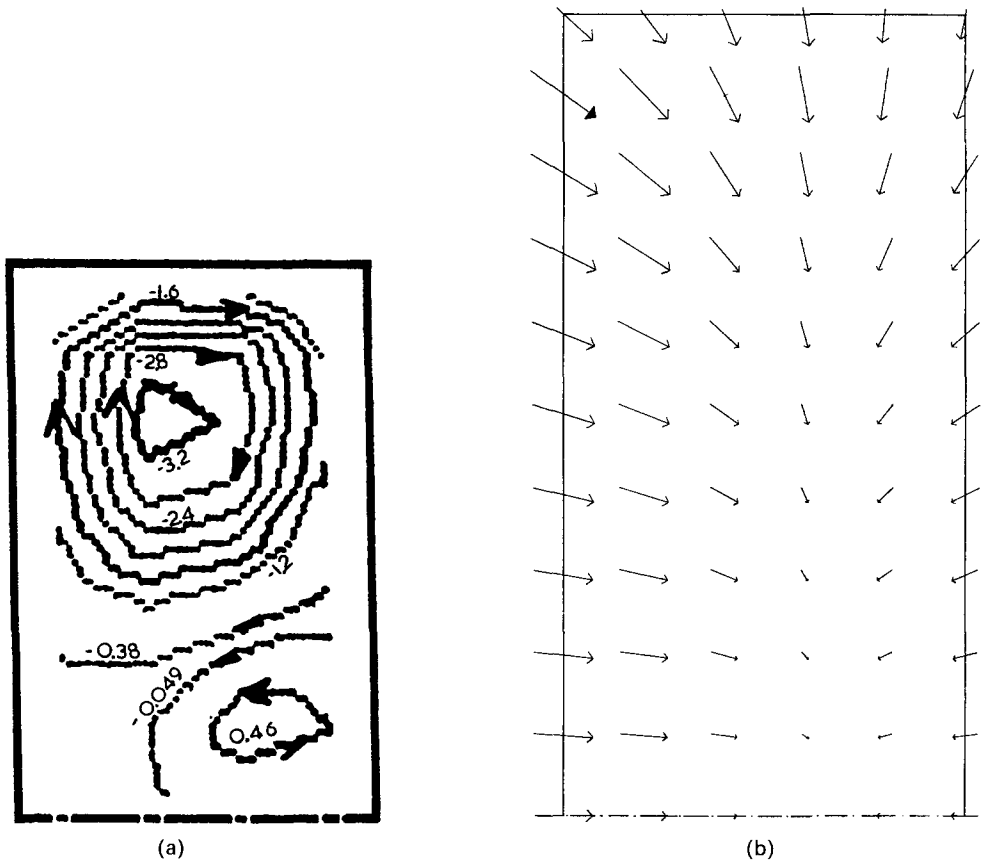

FIG. 16. (a) Computed streamlines for channel of $W = \delta$, $L/2 = 2\delta$. Values in $m^2 s^{-1}$: $I_c = 560$ A, 400 Hz.
(b) Force distribution for channel of $W = \delta$, $L/2 = 2\delta$: $I_c = 560$ A, 400 Hz.

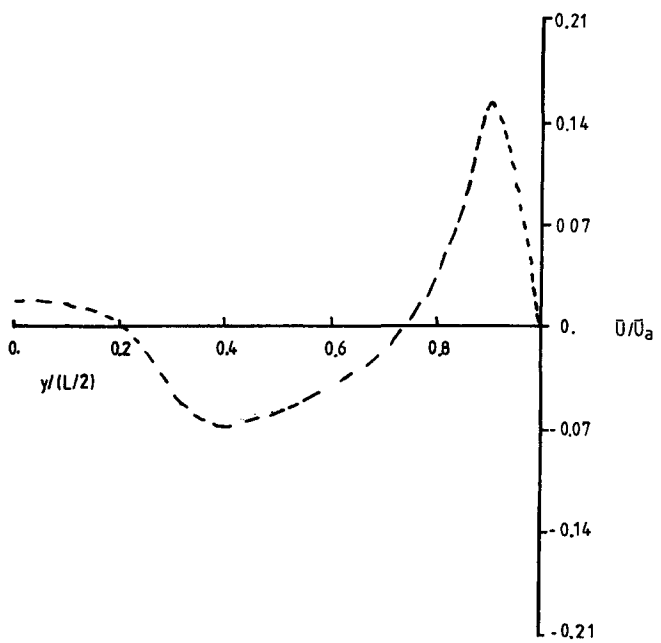

FIG. 17. Axial profile at $x/W = 0.6$ for channel of $W = \delta$, $L/2 = 2\delta$: $I_c = 560$ A, 400 Hz.

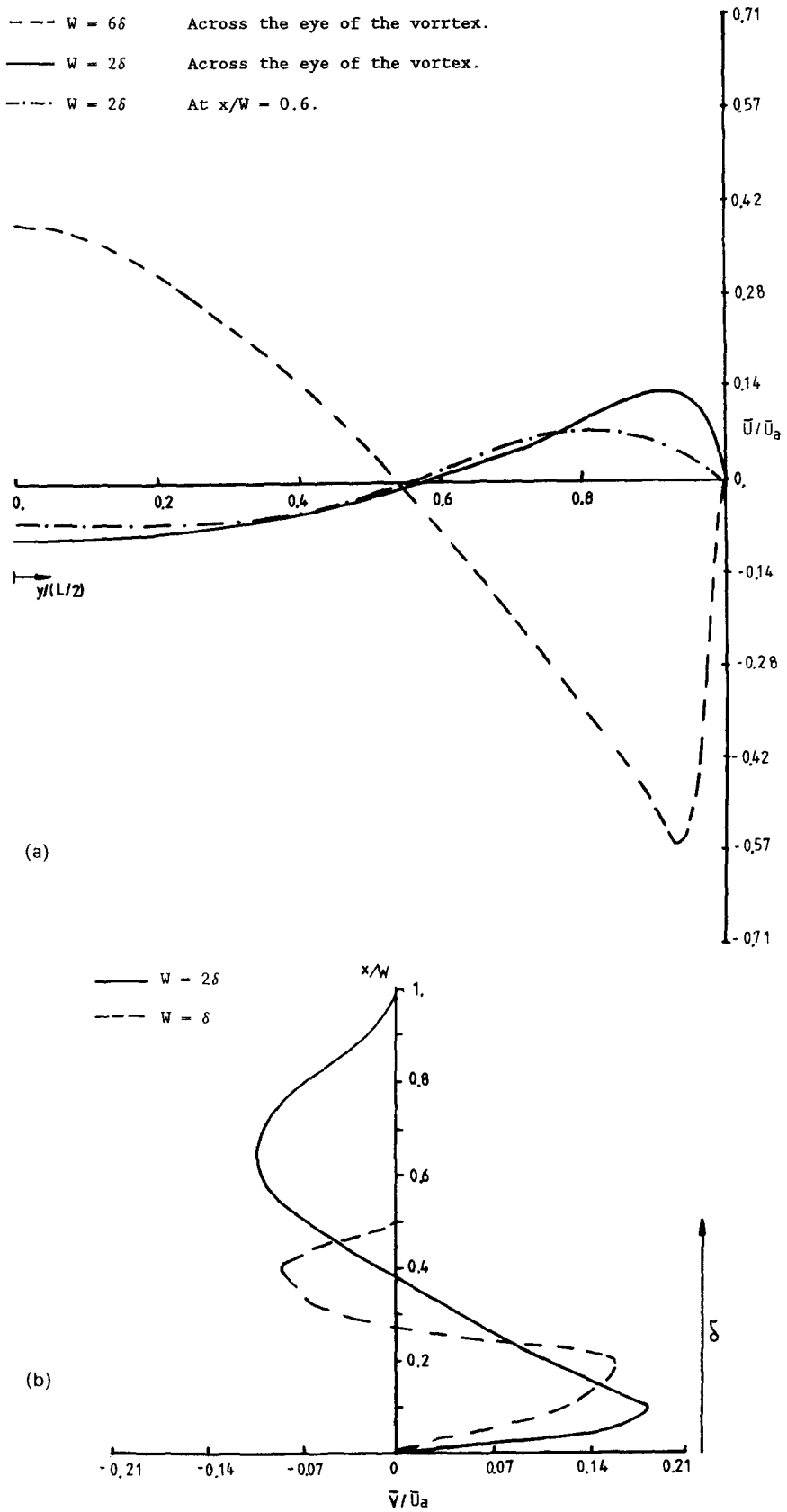

FIG. 18. (a) Axial velocity profiles: $I_c = 560$ A, 400 Hz. (b) Transverse velocity profiles at $y/(L/2) = 0.6$: $I_c = 560$ A, 400 Hz.

culating eddy (Fig. 17). In the last two cases considered the velocities (Figs. 18(a) and (b)) are markedly reduced as compared to those for a channel length of $W = 6\delta$, even the current density is much higher.

For the two cases presented above, approximate analyses for calculating the mean velocities like the one described in the Appendix cannot be used and the overall flow calculation should be performed. In these two cases the flow field cannot be divided into distinct regions because W/δ is of the order of unity and the fluid gains its vorticity in approximately the whole area.

Similar phenomena of flow changing direction of rotation have been observed in the coreless furnaces only when screens are planed on the top or bottom or both corners of the furnace [22], but not different flow patterns when changing the furnace radius.

Figure 19 shows the streamlines for the asymmetric channel. The lower circulation loop has grown at the expense of the upper one. Sharper gradients occur in the region where the forces are greater, in the top eddy. Figure 20 shows the axial velocitiy $\bar{U}$, distribution with y at $x/W = 0.26$, for the cases of symmetric and asymmetric channels.

7. CONCLUSIONS

The distribution of the electromagnetic fields and the resulting recirculating flow on the plane perpendicular to the channel axis, have been studied experimentally and numerically. The flow in the channel is turbulent and, for channels symmetric with respect to the coil, the flow consists of two counter-recirculating eddies. The flow pattern is sensitive to the geometry of the channel, and its position relative to the coil.

Flow measurements and computations showed that the fluid particles gain their vorticity in the regions of strong $\nabla \times (\overline{\mathbf{J} \times \mathbf{B}})$, which is the main force driving the flow.

An approximate analysis based on the balance of the electromagnetic and inertia forces in the channel, does not give a very accurate estimation of the velocity. Simple turbulent models, such as $(k$–$\varepsilon)$ can predict accurately the overall features of the mean flow.

The above calculations give an indication to the channel designer, for the magnitudes of the velocities present in the channel. Of course the overall structure of the flows in CIFs is not yet completely understood. The full three-dimensional structure of the flow, in real furnace geometries needs to be understood in order to be able to predict the mixing mechanism, the lifetime of the inductor, and to design better furnaces. Some preliminary work in this direction has been undertaken by the authors.

Acknowledgements—The authors would like to express their gratitude to Electricity Council Research Centre, SERC, and Wolfson Foundations for financing this work. Also to Dr D. C. Lillicrap and Mr J. Waddington of ECRC for valuable discussions during this work. Furthermore, to FLUENT Co. for permission to use the FLUENT $(k$–$\varepsilon)$ package.

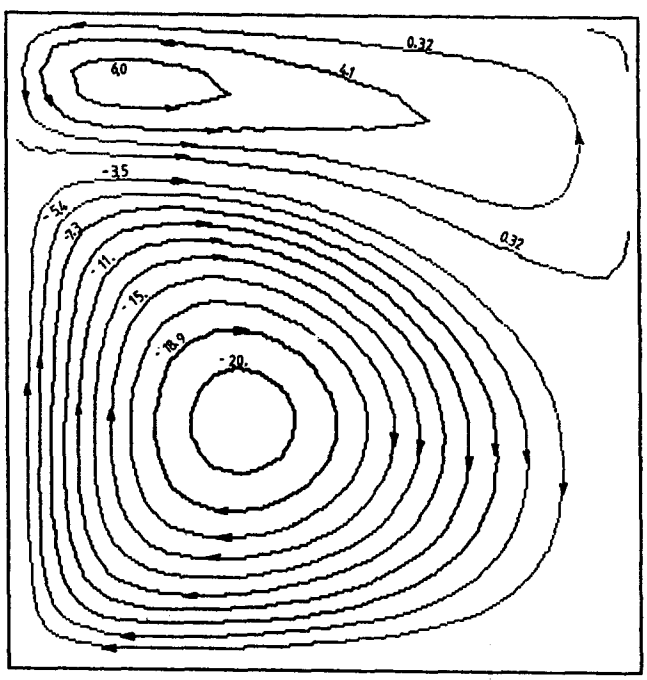

FIG. 19. Computed streamlines for asymmetric channel. Values in $m^2\,s^{-1}$: $I_c = 560$ A, 400 Hz.

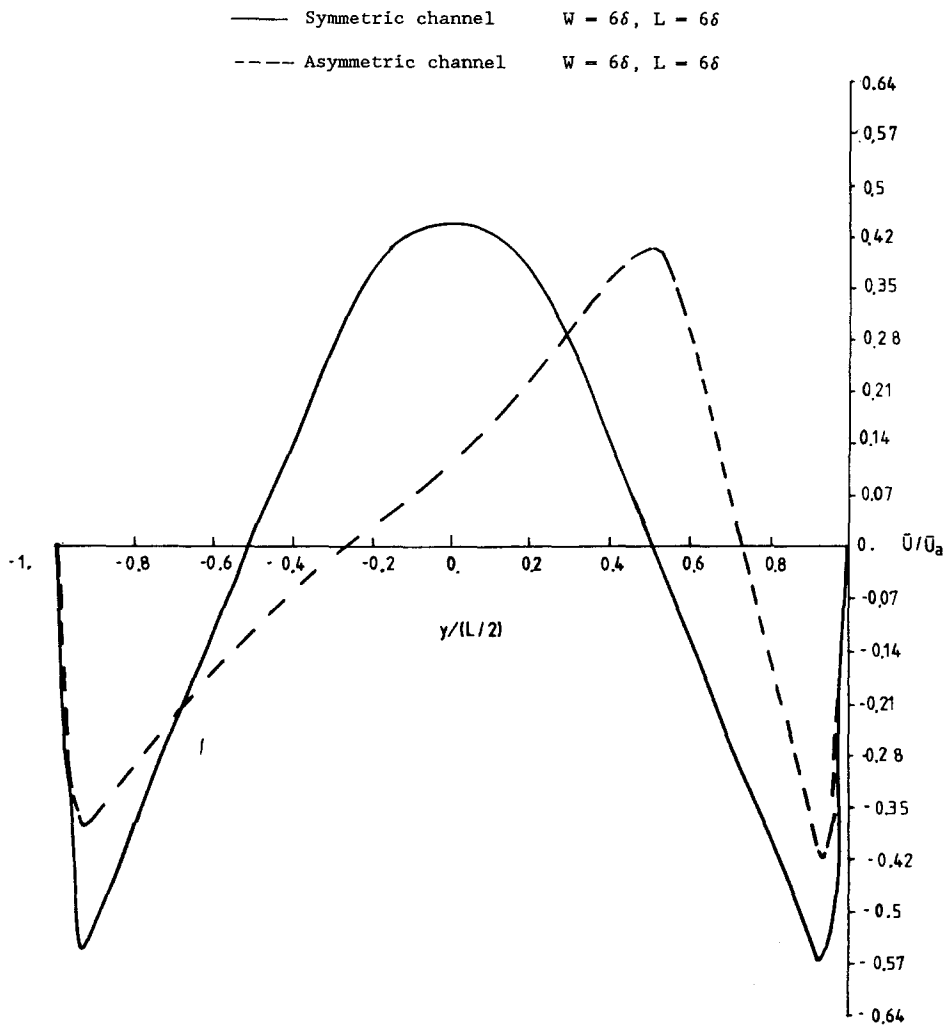

FIG. 20. Axial velocity profiles at $x/W = 0.26$: $I_c = 560$ A, 400 Hz.

REFERENCES

1. A. Moros, J. C. R. Hunt and D. C. Lillicrap, *Prog. Ser. AIAA* **100,** 706–715 (1985).
2. A. Moros, J. C. R. Hunt and D. C. Lillicrap, *Prog. Ser. AIAA* (1988), in press.
3. E. Taberlet and Y. Fautrelle, *Prog. Ser. AIAA* **100,** 725–731 (1985).
4. J. C. R. Hunt and M. Maxey, *Proc. 2nd Beer-sheva Seminar on M.H.D. Flows and Turbulence* (Edited by H. Branover and A. Yakholt), pp. 249–269. Israel University Press (1980).
5. A. Moros, Magnetohydrodynamics of channel induction furnaces, Ph.D., Cambridge University (1986).
6. J. A. Mestel, On the flow in a channel induction furnace, *J. Fluid Mech.* **147,** 431–447 (1984).
7. Becking *et al.*, Swedish Patent 316548 (March 1965).
8. W. Shearman, U.S. Patent 3595979 (July 1971).
9. R. A. Sommer, *Proc. Biennial Conf. on Electric Heating in Industry*, IEEE, Toronto (1975).
10. R. D. Langman *et al.*, ECRC Report R495 (April 1972).
11. I. E. Butsenieks *et al.*, *Magnetohydrodynamics* **16,** 324–330 (1980).
12. A. V. Arefev *et al.*, Heat and mass transfer intensification in channel induction furnaces, Riga Report LAFI023, Trans., ECRC Report OA3268 (1985).
13. J. Szekely and W. Chang, *Ironmaking Steelmaking* No. 3, 190–204 (1977).
14. E. P. Tarapore *et al.*, *Metall. Trans.* **8B,** 179–184 (1977).
15. A. Moros, Drag anemometry for measuring velocities in electromagnetically driven flows!, *J. Phys. E.* **19,** 1050–1054 (1986).
16. C. Trakas *et al.*, *Proc. IUTAM Cambridge Metal Society* (Edited by H. K. Moffatt and M. R. E. Proctor) (1984).
17. W. Rodi, Turbulence models and their applications in hydraulics, IAHR, State of the art paper (1984).
18. J. W. Waddington, A finite element code for the computation of sinusoidal eddy currents, Electricity Council Research Centre, Capenhurst, Chester, U.K. (1986).
19. S. V. Patankar, *Numer. Heat Transfer and Fluid Flow.* Hemisphere, Washington DC (1980).
20. B. E. Launder and D. B. Spalding, *Comput. Meth. Appl. Mech. Engng.* **3,** 269–289 (1974).
21. D. J. Moore and J. C. R. Hunt, *Proc. IUTAM Cambridge Metal Society* (Edited by H. K. Moffatt and M. R. E. Proctor) (1984).

22. C. H. Vives and R. Ricou, *Metall. Trans.* **16B**, 227–235 (1985).
23. R. Moreau, Applications metalurgique des Magnetohydrodynamique, *Proc. IUTAM Conf.*, Toronto (1980).
24. S. Sivasegaram and J. H. Whitelaw, Imperial College Report, Dept. of Mech. Engng, Fluid Section FS/84/26 (June 1984).
25. D. C. Lillicrap, *Elektrowarme Int.* **44**, B116–B122 (1986).
26. S. Hellsing and G. Tallback, *Conf. Proc. of Light Metals, 111th AIME Annual Meeting*, Dallas, Texas, 14–18 February (Edited by J. E. Anderson) (1982).

APPENDIX: ORDER OF MAGNITUDE ANALYSIS FOR APPROXIMATE ESTIMATION OF THE VELOCITY

The balance of forces in the melt are described by the time-averaged turbulent Navier–Stokes equation (7)

$$(\mathbf{U}\cdot\nabla)\mathbf{U} = \frac{1}{\rho}\nabla p + \frac{1}{\rho}\nabla\cdot\tilde{\tau} + \frac{1}{\rho}\overline{(\mathbf{J}\times\mathbf{B})} \tag{A1}$$

where ∇p is the pressure gradient and $\tilde{\tau}$ the Reynolds stress tensor $\overline{\rho u_i u_j}$. It is assumed that ρ is uniform and, as has been mentioned in Section 1, the buoyancy forces are negligible by comparison to $\overline{(\mathbf{J}\times\mathbf{B})}$. The pressure term is eliminated by taking the curl of equation (A1). Then in terms of vorticity we have

$$\nabla\times(\mathbf{U}\cdot\nabla)\mathbf{U} = \nabla\times\left(\frac{1}{\rho}\nabla\cdot\tilde{\tau}\right) + \frac{1}{\rho}(\nabla\times\overline{(\mathbf{J}\times\mathbf{B})}). \tag{A2}$$

Following the discussion in Section 5, the fluid gains most of its vorticity as it passes through the corner region (Fig. A1) and then develops as a turbulent wall jet along the inner wall. Some of the streamlines probably do not pass through that region but the fluid gains vorticity due to diffusion. Still along the inner wall in the region near the axis of symmetry the electromagnetic forces rotate the fluid particles in the opposite direction and consequently the velocity profile flattens out (not observed in the coreless furnaces). In the corner region in Fig. A1, where $\Delta x \approx \Delta y$, the terms in equation (A2) have the following order of magnitude.

Shear stress

The stress term is composed from the viscous term and the turbulent Reynolds stress term

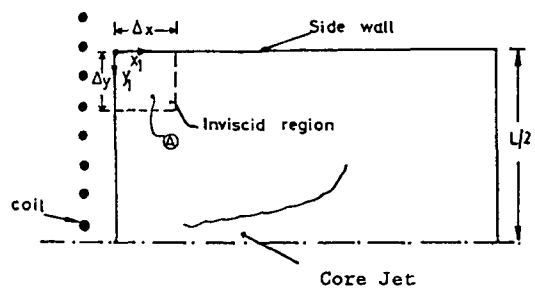

FIG. A1. Schematic diagram of the channel.

$$\nabla\times\nabla\cdot\tilde{\tau} \approx \rho\left(\frac{u_+^2}{\Delta x^2} + \frac{u'^2}{\Delta x^2}\right)$$

where $u_+ = (\tau_0/\rho)^{1/2}$, $\tau_0 = \nu[\partial U/\partial y]_w$ and u' is the r.m.s. turbulent velocity.

Inertia term

$$\rho\nabla\times(\mathbf{U}\cdot\nabla)\mathbf{U} \approx \frac{\rho U^2}{\Delta x^2}.$$

Electromagnetic term

$$\nabla\times\overline{(\mathbf{J}\times\mathbf{B})} \approx \frac{B_0^2}{\mu\Delta x^2}. \tag{A3}$$

In the corner region A of Fig. A1 the shear term is much smaller than the inertial and the electromagnetic term, except in the viscous sublayer which is of the order of ν/u_+. Therefore, there is a balance between the inertial and the electromagnetic term so as equation (A2) reduces to

$$\frac{\partial}{\partial x}(U\Omega) + \frac{\partial}{\partial y}(V\Omega) \approx \frac{1}{\rho}\nabla\times\overline{(\mathbf{J}\times\mathbf{B})} \tag{A4}$$

where $\Omega = \partial V/\partial x - \partial U/\partial y$. Integrating over the corner region A using local coordinates (x_1, y_1) we obtain

$$\int_0^{\Delta x}\int_0^{\Delta y}\left(\frac{\partial}{\partial x}(U\Omega) + \frac{\partial}{\partial y}(V\Omega)\right)\mathrm{d}y\,\mathrm{d}x \approx \frac{1}{\rho}\int_0^{\Delta x}\int_0^{\Delta y}\nabla\times\overline{(\mathbf{J}\times\mathbf{B})}\,\mathrm{d}y\,\mathrm{d}x. \tag{A5}$$

The boundary conditions for the mean velocity are

$$\text{at } y = 0,\ V = 0 \text{ and at } x = 0,\ U = 0.$$

Because of the mixing of vorticity of opposite sign between the two eddies in the channel, by the time the fluid returns to the region of high electromagnetic forces has small vorticity. It gains most of its vorticity due to the action of $\nabla\times\overline{(\mathbf{J}\times\mathbf{B})}$. Equation (A5) subject to the boundary conditions becomes

$$\int_0^{\Delta y} U\Omega\,\mathrm{d}y + \int_0^{\Delta x} V\Omega\,\mathrm{d}x = \frac{1}{\rho}\int_0^{\Delta x}\int_0^{\Delta y}\nabla\times\overline{(\mathbf{J}\times\mathbf{B})}\,\mathrm{d}y\,\mathrm{d}x. \tag{A6}$$

Along the inner wall where the streamlines are parallel to the wall, $V \gg U$ and $\Omega \approx \partial V/\partial x$. Therefore, the first term on the left-hand side of equation (A6) is negligible. Hence equation (A6) becomes

$$-\int_0^{\Delta x} V\frac{\partial V}{\partial x}\mathrm{d}x \approx \frac{1}{\rho}\int_0^{\Delta x}\int_0^{\Delta y}\nabla\times\overline{(\mathbf{J}\times\mathbf{B})}\,\mathrm{d}y\,\mathrm{d}x \tag{A7}$$

or

$$-V^2(x) \approx \frac{2}{\rho}\int_0^{\Delta x}\int_0^{\Delta y}\nabla\times\overline{(\mathbf{J}\times\mathbf{B})}\,\mathrm{d}y\,\mathrm{d}x. \tag{A8}$$

Dividing the corner region into small strips and using the computed values of $\nabla\times\overline{(\mathbf{J}\times\mathbf{B})}$ the velocity V was evaluated numerically and the results are shown in Fig. 10.

ECOULEMENTS DE RECIRCULATION DANS LA SECTION DROITE D'UN CANAL DE FOUR A INDUCTION

Résumé—On étudie les écoulements de recirculation dans les fours à canal pour comprendre et prédire leur efficacité de mélange et leurs aspects désavantageux tels que le blocage du canal par des matériaux non métalliques et par l'érosion du réfractaire. Ces aspects réduisent leur durée de vie. On a divisé l'étude en deux parties. Dans la première, donnée ici, on analyse l'écoulement bidimensionnel dans un modèle de laboratoire simulant une jambe du canal. Il s'agit d'un réservoir carré 150×150 mm, contenant 90 kg de mercure et d'un générateur à 400 Hz. La distribution du flux **B** est mesurée par des enroulements. On en déduit la distribution de $(\mathbf{J} \times \mathbf{B})$ et de $\nabla \times (\mathbf{J} \times \mathbf{B})$. Les résultats sont comparés avec des solutions des équations de Maxwell obtenues à partir d'un code d'éléments finis. C'est un problème découplé. On résout les équations de Maxwell puis les résultats de $\mathbf{J} \times \mathbf{B}$ permettent de résoudre les équations de Navier–Stokes. L'écoulement moyen et l'intensité de turbulence de l'écoulement de recirculation sont mesurés et comparés avec des solutions obtenues à partir d'un code $(k-\varepsilon)$, et avec des analyses approchées basées sur un bilan des termes $\nabla \times (\mathbf{J} \times \mathbf{B})$ et d'inertie. Des expériences numériques montrent comment la configuration de l'écoulement dans la section droite du canal change avec les modifications (i) de la géométrie du canal ou (ii) la longueur de l'enroulement et (iii) la position de l'enroulement par rapport au canal.

RÜCKSTRÖMUNGEN IM KANALQUERSCHNITT EINES INDUKTIONSOFENS

Zusammenfassung—Um die Mischungswirkung von Rückströmungen im Kanalquerschnitt eines Induktionsofens zu verstehen und zu berechnen, müssen die vorhandenen Rückströmungen genauer untersucht werden. Dabei gilt es auch, deren Nachteile zu erfassen, welche zu einer Reduzierung der Standzeit führen, z. B. das Blockieren des Kanals durch nichtmetallisches Material und den Materialabtrag durch Abbrand. Um das physikalische Prinzip, das die Strömung antreibt, besser zu verstehen, haben wir unsere Untersuchungen in zwei Teile gegliedert. Im ersten Teil, welcher in dieser Veröffentlichung beschrieben wird, analysieren wir das zweidimensionale Strömungsfeld an einem Labormodell. Das Modell besteht aus einem quadratischen Tank (150×150 mm), welcher 90 kg Quecksilber enthält und von einem 400 Hz Generator angetrieben wird. Die Verteilung des Induktionsstroms (**B**) wurde mit Hilfe von Meßspulen gemessen. Daraus wurden die Verteilungen von $(\mathbf{J} \times \mathbf{B})$ und der Rotation $\nabla \times (\mathbf{J} \times \mathbf{B})$ abgeschätzt. Diese Verteilungen wurden mit einer Computersimulation nach der Methode der finiten Elemente verglichen. Das Problem wurde dadurch entkoppelt, daß das sich aus der Lösung der Maxwell-Gleichungen ergebende $(\mathbf{J} \times \mathbf{B})$ zur Lösung der Navier–Stokes-Gleichung herangezogen wurde. Der mittlere Induktionsstrom und die Intensität der turbulenten Rückströmung wurden gemessen und mit den Simulationsergebnissen des $(k$–$\varepsilon)$-Modells verglichen. Dieses Modell ist eine Näherung, die auf dem Gleichgewicht zwischen $\nabla \times (\mathbf{J} \times \mathbf{B})$ und den Trägheitstermen beruht. Numerische Experimente zeigen, wie sich das Strömungsmuster im Querschnitt des Kanals in Abhängigkeit von der Kanalgeometrie (i), der Spulenlänge (ii) oder der Positionierung der Spule am Kanal (iii) ändert.

РЕЦИРКУЛИРУЮЩИЕ ТЕЧЕНИЯ В ПОПЕРЕЧНОМ СЕЧЕНИИ ИНДУКЦИОННОЙ ПЕЧИ КАНАЛЬНОГО ТИПА

Аннотация—Для понимания и расчета эффективности смешения и отрицательных явлений в рециркулирующих потоках, таких как загромождение канала неметаллическими материалами и эрозия огнеупора, необходимо исследование рециркулирующих течений в индукционных печах канального типа. Вышеупомянутые явления сокращают срок службы печей. Чтобы лучше понять физические механизмы течения, исследование проводится в два этапа. В первом, описанном в настоящей работе, рассматривается двумерный поток в лабораторной модели, имитирующей одно колено канала. Модель представляла собой бак квадратного сечения со стороной 150 мм, содержащий 90 кГ ртути и питаемый высокочастотным генератором (400 Гц). Распределение потока индукции **B** измерялось с помощью индукционных катушек. Таким образом были получены распределение $(\mathbf{J} \times \mathbf{B})$ и ротор $\nabla \times (\mathbf{J} \times \mathbf{B})$. Полученные результаты сравнивались с численными решениями уравнений Максвелла, полученными методом конечных элементов. Задача решалась в несопряженной постановке: сначала решаются уравнения Максвелла, а затем по решениям для $(\mathbf{J} \times \mathbf{B})$ решались уравнения Навье–Стокса. Измерены осредненные значения скорости и интенсивность турбулентности рециркулирующего потока, данные сравниваются с решениями, полученными на основе $(k$–$\varepsilon)$-модели, и приближенного анализа, основанного на балансе между $\nabla \times (\mathbf{J} \times \mathbf{B})$ и инерционными членами. Численные эксперименты показывают как режим течения в поперечном сечении канала изменяется с изменениями геометрии канала, длины катушки и положения катушки относительно канала.